

Optimized Designs for Very Low Temperature Massive Calorimeters

Matt Pyle,^{1,*} Enectali Figueroa-Feliciano,² and Bernard Sadoulet¹

¹*Physics Department, University of California Berkeley*

²*Physics Department, Massachusetts Institute of Technology*

(Dated: March 13, 2015)

The baseline energy-resolution performance for the current generation of large-mass, low-temperature calorimeters (utilizing TES and NTD sensor technologies) is > 2 orders of magnitude worse than theoretical predictions. A detailed study of several calorimetric detectors suggests that a mismatch between the sensor and signal bandwidths is the primary reason for suppressed sensitivity. With this understanding, we propose a detector design in which a thin-film Au pad is directly deposited onto a massive absorber that is then thermally linked to a separately fabricated TES chip via an Au wirebond, providing large electron-phonon coupling (i.e. high signal bandwidth), ease of fabrication, and cosmogenic background suppression. Interestingly, this design strategy is fully compatible with the use of hygroscopic crystals (NaI) as absorbers. An 80-mm diameter Si light detector based upon these design principles, with potential use in both dark matter and neutrinoless double-beta decay, has an estimated baseline energy resolution of 0.35 eV, $20\times$ better than currently achievable. A 1.75 kg ZnMoO₄ large-mass calorimeter would have a 3.5 eV baseline resolution, $1000\times$ better than currently achieved with NTDs with an estimated position dependence $\frac{\Delta E}{E}$ of 6×10^{-4} , near or below the variations found in absorber thermalization in ZnMoO₄ and TeO₂. Such minimal position dependence is made possible by forcing the sensor bandwidth to be much smaller than the signal bandwidth. Further, intrinsic event timing resolution is estimated to be $\sim 170 \mu\text{s}$ for 3 MeV recoils in the phonon detector, satisfying the event-rate requirements of large $Q_{\beta\beta}$ next-generation neutrinoless double-beta decay experiments. Quiescent bias power for both of these designs is found to be significantly larger than parasitic power loads achieved in the SPICA/SAFARI infrared bolometers.

PACS numbers: 95.55.Vj, 95.35.+d, 29.40.Vj, 29.40.Wk

I. MOTIVATION

The success of experiments that use massive very low-temperature calorimeters (e.g. CRESST [1], CUORE [2], EDELWEISS [3] and CDMS [4]) in rare event searches is quite natural since phonon vibrational modes with energy above $k_b T$ freeze out and thus do not contribute to the crystal heat capacity, leading to T^3 heat capacity scaling for semi-conducting and insulating crystals. Consequently, detectors with a large active mass and excellent energy resolution should be possible. To reiterate the utility of this natural scaling law: for a given energy deposition, a giant 1-tonne Si crystal at 10 mK will have the same temperature change as 1 g at 1 K.

At low temperature (~ 100 mK), calorimetry based on Transition Edge Sensor (TES) technology is quite mature and has been used for energy measurement at virtually all energy scales from infrared-photon (~ 100 meV) [5] to alpha detection (~ 10 MeV) [6]. The measured energy resolution of well designed devices throughout this regime roughly matches the theoretical expectation of

$$\sigma_E^2 = \frac{4k_b T_c^2 C}{\alpha} \sqrt{\frac{n\mathcal{F}(T_c, T_b)\xi(I)}{1 - \frac{T_b^n}{T_c^n}}} \quad (1)$$

where T_c is the superconducting transition temperature

of the TES, $\alpha \left(\frac{T}{R} \frac{\partial R}{\partial T} \right)$ is the unitless sensitivity parameter, and the unitless terms within the square root all combine to usually be of order 2 [7].

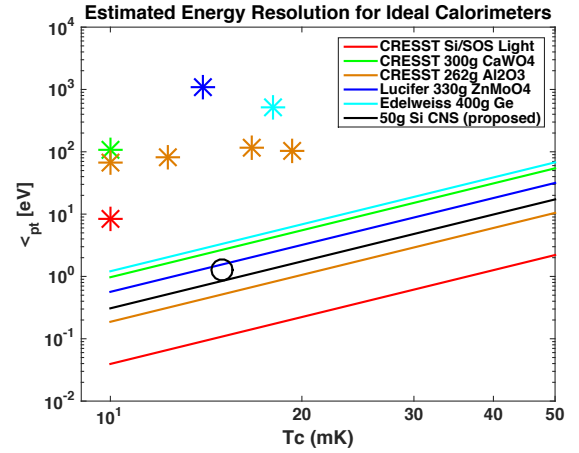


FIG. 1. The naively estimated intrinsic energy resolution (Eq. 1) as a function of T for a variety of different massive calorimeters versus their actual device performance (stars) [1, 3, 8–10]. The plotted 50 g Si coherent neutrino scattering resolution (black circle) is simply a more detailed performance estimate by [11], taking into account internal device thermal conductances and other non-ideal device characteristics, that shows rough agreement with the simpler scaling law estimates.

In Fig. 1, we benchmark the measured performance of the current generation of massive calorimeters oper-

* mpyle1@berkeley.edu

ating near 10 mK (stars) and a detailed proposal for a 50 g Si coherent neutrino scattering detector [11] (black circle) against the theoretical scaling law of Eq. 1 assuming that the total heat capacity of the detector is $2\times$ that of the absorber and that $\alpha = 20$ (values of 10–500 are common). Unfortunately we find that the energy-resolution performance of all current experiments is 2–3 orders of magnitude worse than expected from Eq. 1. Consequently, either there are substantial experimental limitations at very low temperature that are not taken into account in Eq. 1, and [11], or the current generation of massive calorimeters could be significantly improved.

To gain insight into this energy resolution discrepancy, we will carefully study both the dynamics and noise of the original [8] and composite [1] CRESST phonon detectors as well as other calorimeters and then motivate and develop 6 design criteria that are applicable to very low-temperature massive detectors:

1. The signal bandwidth (frequency scale at which energy transfers from the absorber to the sensor) must be greater than or equal to sensor bandwidth,
2. The transition edge sensor (TES) must not phase separate,
3. The sensor bandwidth must be larger than the $1/f$ noise threshold,
4. The sensor bandwidth must be large enough to satisfy event rate requirements, and
5. Microfabrication techniques should be used only on standard thin wafers.
6. For applications that require minimal position dependence of energy estimators, we require that that signal bandwidth \gg than the sensor bandwidth.

Finally, we present 2 prototype designs that simultaneously achieve all of these design requirements: a single-photon-sensitive light detector and a 1.75 kg ZnMoO_4 double-beta decay detector.

II. SIMULATING CRESST PHONON DETECTOR

Modeling of complex calorimeters with multiple coupled thermal degrees of freedom (DOF) like the CRESST phonon detector has been a very active area of research, particularly within the x-ray and gamma-ray TES communities [15–18]. Thus, we need only apply mature strategies, being careful to follow the conventions of [7]. This is made even easier by the fact that CRESST has already modeled the dynamics of their detectors [12, 19, 20] and even attempted to simulate noise [12]; so we will concentrate in particular on developing analytical simplifications and physical intuition, neither of which has yet been done.

CaWO ₄ absorber			
V_a	Absorber volume		$\pi \times 2^2 \times 4 \text{cm}^3$ [12]
M_a	Absorber mass		300 g [12]
C_a	Absorber heat capacity	$\Gamma_{\text{CaWO}_4} V_a T^3$	$132 \frac{\text{pJ}}{\text{K}}$ @10mK
W TES			
A_t	Cross sectional area		7.5mmx200nm[12]
l_t	Length		5.9 mm [12]
V_t	Volume	$A_t l_t$	$8.9 \times 10^{-3} \text{mm}^3$
C_t	Heat capacity	$f_{sc} \Gamma_W V_t T$	$22.7 \frac{\text{pJ}}{\text{K}}$ @10mK
P_{ta}	Power flow from TES to absorber	$\Sigma_{epW} V_t (T_t^n - T_a^n)$	
G_{ta}	Thermal conductance between TES and absorber	$\frac{\partial P_{ta}}{\partial T_t}$	$142 \frac{\text{pW}}{\text{K}}$ @10mK
$G_{t \text{int}}$	internal TES conductance	$\frac{L_{wf}}{\rho W} \frac{A_t}{l_t/2} T$	$1.63 \frac{\text{nW}}{\text{K}}$
R_n	TES normal resistance	$\rho W \frac{l_t}{A_t}$	300 m Ω [12]
T_c	Transition temperature		~ 10 mK
Au wirebond: thermal link to bath			
T_b	Bath temperature		6 mK [13]
l_{tb}	\sim Wirebond length		2 cm [9]
A_{tb}	Cross sectional area		$\pi \times 12.5^2 \mu\text{m}^2$ [12]
P_{tb}	Power flow from TES to bath	$\frac{v_{fd} \Gamma_{Au} A_{tb}}{6 l_{tb}} (T_t^2 - T_b^2)$	19.2 pW
G_{tb}	Thermal conductance from TES to bath	$\frac{\partial P_{tb}}{\partial T_t}$	7.5 nW/K @10mK
Electronics properties			
L	Inductance (SQUID+ parasitic)		350 nH [14]
R_l	Load resistor (shunt+ parasitic)		40 m Ω [14]
T_l	Temperature of R_l		10mK [14]
S_{ISQUID}	SQUID Current Noise		$1.2 \text{ pA}/\sqrt{\text{Hz}}$ [14]

TABLE I. Estimated CRESST-II phonon-detector device parameters using the material properties in Appendix A.

A. Dynamics

The original (non-composite) CRESST-II phonon detector is a large 300 g cylindrical CaWO_4 crystal with a W TES ($T_c \approx 10$ mK) and all of its required accessories (bonding pads, Al bias rails) fabricated directly upon its surface, as shown in Fig. 2 [12]. Unfortunately, even after such painstaking fabrication efforts, the thermal coupling between the TES and the large mass absorber, G_{ta} , is still $50\times$ smaller than the thermal conductance between the TES and the bath via the direct electronic coupling of the Au wirebond, G_{tb} (cf. Table. I). This is because the W electronic system (sensor) and the phonon system of the TES and absorber almost completely decouple at very low temperatures since the thermal power flow scales as T^5 .

From a modeling perspective, the primary consequence

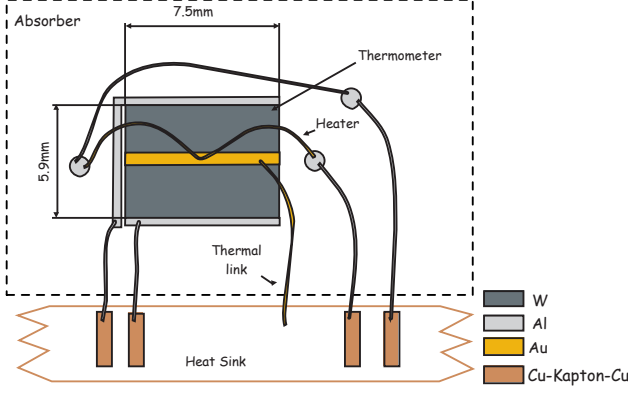


FIG. 2. Schematic of the TES and its connections on the original CRESST-II phonon detector [12].

is that any realistic device simulation requires separate thermal DOF for the absorber, T_a , and the TES, T_t , in addition to modeling the current flowing through the TES I_t which will be measured through an inductively coupled SQUID. Thus in a way similar to CRESST [19], we will model the system as 3 coupled non-linear differential equations

$$\begin{aligned} L \frac{dI_t}{dt} &= V_b - I_t (R_l + R_t(T_t, I_t)) + \delta V \\ C_t \frac{dT_t}{dt} &= I_t^2 R_t(T_t, I_t) - P_{tb}(T_t, T_b) - P_{ta}(T_t, T_a) + Q + \delta P_t \\ C_a \frac{dT_a}{dt} &= -P_{ab}(T_a, T_b) + P_{ta}(T_t, T_a) + \delta P_a \end{aligned} \quad (2)$$

where δV is a small voltage-bias excitation on top of the DC voltage-bias V_b that we will use to model Johnson noise as well as the small signal dynamics of the detector. Likewise, δP_t and δP_a are power excitations into the TES and absorber respectively. This model can also be seen diagrammatically in Fig. 3. Variable definitions and estimated sizes can be found in Table I. One relatively unique feature of the CRESST design is the capability to directly heat the TES electronic system through an additional heater circuit (Q). When held constant, this is effectively equivalent to being able to easily vary the bath temperature T_b on a detector by detector basis.

Taylor expanding to first order around the operating point, $[I_{to}, T_{to}, T_{ao}]$ and then Fourier transforming, these equations simplify to

$$\begin{bmatrix} j\omega + \frac{R_{to}(1+\beta)+R_l}{L} & \frac{I_{to}R_{to}\alpha}{LT_{to}} & 0 \\ -\frac{I_{to}R_{to}(2+\beta)}{C_t} & j\omega + \frac{I_{to}^2R_{to}\alpha - G_{ta} - G_{tb}}{C_t} & -\frac{G_{ta,a}}{C_t} \\ 0 & -\frac{G_{ta}}{C_a} & j\omega + \frac{G_{ta,a}+G_{ab}}{C_a} \end{bmatrix} \begin{bmatrix} \Delta I_t(\omega) \\ \Delta T_t(\omega) \\ \Delta T_a(\omega) \end{bmatrix} = \begin{bmatrix} \frac{\delta V(\omega)}{L} \\ \frac{\delta P_t(\omega)}{C_t} \\ \frac{\delta P_a(\omega)}{C_a} \end{bmatrix} \quad (3)$$

which in the pertinent limit of $L \rightarrow 0$ can be simplified to only thermal DOF

$$\begin{bmatrix} j\omega + (\mathcal{L}_{2D}+1)\frac{G_{ta}+G_{tb}}{C_t} & -\frac{G_{ta,a}}{C_t} \\ -\frac{G_{ta}}{C_a} & j\omega + \frac{G_{ta,a}+G_{ab}}{C_a} \end{bmatrix} \begin{bmatrix} \Delta T_t \\ \Delta T_a \end{bmatrix} = \begin{bmatrix} \frac{\delta P_t}{C_t} + \frac{I_{to}R_{to}(2+\beta)\delta V}{C_t(R_l+R_{to}[1+\beta])} \\ \frac{\delta P_a}{C_a} \end{bmatrix} \quad (4)$$

where

$$\delta I_t = \frac{-I_{to}R_{to}\alpha}{(R_l + R_{to}[1 + \beta])T_{to}} \delta T_t + \frac{1}{R_l + R_o[1 + \beta]} \delta V \quad (5)$$

As is standard, β or $\frac{I_{to}}{R_{to}} \frac{\partial R_t}{\partial I_t}(T_{to}, I_{to})|_{T_t}$ characterizes the unwanted dependence of R_t on the current. Also note that we have generalized Irwin's loop gain parameter \mathcal{L}_I to

$$\mathcal{L}_{2D} = \alpha \frac{R_{to} - R_l}{R_{to}(1 + \beta) + R_l} \frac{I_{to}^2 R_{to}}{(G_{tb} + G_{ta})T_{to}} \quad (6)$$

to account for the 2 thermal DOF as well as the fact that CRESST has purposely chosen to use a load resistor (R_l) that is of similar magnitude to R_{to} to suppress electro-thermal feedback. Finally, due to the possibility that T_{to} and T_{ao} could be macroscopically different, the thermal conductances $\frac{\partial P_{ta}}{\partial T_t}$ and $\frac{\partial P_{ta}}{\partial T_a}$ could have different values

and consequently we define

$$\begin{aligned} G_{ta,a} &= \frac{\partial P_{ta}}{\partial T_a} \\ &= \frac{\partial P_{ta}}{\partial T_t} \left(\frac{T_a}{T_t} \right)^{n_{ep}-1} \\ &= G_{ta} \left(\frac{T_a}{T_t} \right)^{n_{ep}-1} \end{aligned} \quad (7)$$

Inversion of the generalized impedance matrix, M_{2D} , found in Eq. 4 leads to the current transfer functions for the thermal power response for direct heating into

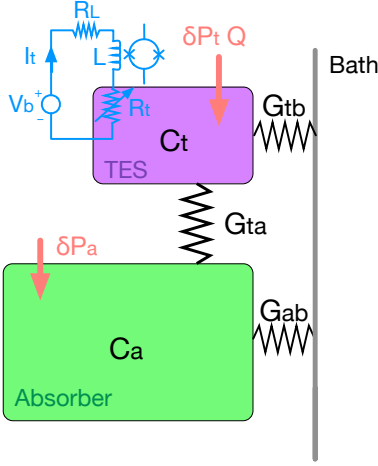


FIG. 3. Simplified model of the CRESST phonon and light detectors with 2 thermal DOF as well as the voltage-bias and current readout circuit

the TES

$$\begin{aligned} \frac{\partial I_t}{\partial P_t} &= \frac{-I_{to}R_{to}}{R_l+R_{to}(1+\beta)} \frac{\alpha}{C_t T_t} M_{2D(1,1)}^{-1}(\omega) \\ &\sim \frac{-I_{to}R_{to}}{R_l+R_{so}(1+\beta)} \frac{\alpha}{(\mathcal{L}_{2D}+1)} \frac{1}{(G_{tb}+G_{ta}) T_t} \frac{1}{1+j\omega/\omega_{eff}} \\ &\sim \frac{-1}{I_{to}(R_{to}-R_l)} \frac{\mathcal{L}_{2D}}{\mathcal{L}_{2D}+1} \frac{1}{1+j\omega/\omega_{eff}} \end{aligned} \quad (8)$$

and into the absorber

$$\begin{aligned} \frac{\partial I_t}{\partial P_a} &= \frac{-I_{to}R_{to}}{R_l+R_{to}(1+\beta)} \frac{\alpha}{C_a T_t} M_{2D(1,2)}^{-1}(\omega) \\ &\sim \frac{\partial I_t}{\partial P_t} \left(\frac{G_{ta,a}}{G_{ta,a}+G_{ab}} \right) \left(\frac{1}{1+j\omega/\omega_{ta}} \right) \end{aligned} \quad (9)$$

where

$$\begin{aligned} \omega_{eff} &= (\mathcal{L}_{2D}+1) \frac{G_{ta}+G_{tb}}{C_t} + \frac{1}{\mathcal{L}_{2D}+1} \frac{G_{ta,a}}{G_{ta}+G_{tb}} \frac{G_{ta}}{C_a} + \dots \\ \omega_{ta} &= \frac{G_{tb}+G_{ta,a}}{C_a} - \frac{1}{\mathcal{L}_{2D}+1} \frac{G_{ta,a}}{G_{ta}+G_{tb}} \frac{G_{ta}}{C_a} + \dots \end{aligned} \quad (10)$$

All of the approximations shown are valid only for the pertinent limiting case where G_{ta} and $G_{ab} \ll G_{tb}$ (cf. Table I).

Qualitatively, the last term of Eq. 9, which is an additional pole that suppresses the bandwidth of $\frac{\partial I_t}{\partial P_a}$ relative to $\frac{\partial I_t}{\partial P_t}$, is due to the fact that thermal energy must be transported across the tiny G_{ta} before it is seen by the TES. Likewise, the middle term of Eq. 9 is a constant suppression factor because a portion of δP_a is shunted through G_{ab} . This suppression should be small for the CRESST phonon detector. However, for the CRESST light detector, the Au wirebond pad on the substrate has

an electron-phonon coupling that is larger than that of the W TES, and consequently this factor is significant [12]. Another detector with significant shunting is found in CUORE where the vast majority of the absorber thermal signal flows through G_{ab} [21].

Both the $\frac{\partial I_t}{\partial P_t}$ (Eq. 8) and $\frac{\partial I_t}{\partial P_a}$ (Eq. 9) transfer functions are important for understanding the signal response of massive calorimeters, because some of the high-energy athermal phonons produced by a particle recoil in the absorber may be collected and thermalized within the TES (δP_t) before they thermalize within the absorber (δP_a), since the electron-phonon coupling varies so significantly with phonon energy and temperature. Consequently, a true particle recoil within the absorber should be modeled within our 2 thermal DOF system as

$$\begin{aligned} \frac{\partial I_t}{\partial E_\gamma} &= \frac{\partial I_t}{\partial P_t} \frac{\partial P_t}{\partial E_\gamma} + \frac{\partial I_t}{\partial P_a} \frac{\partial P_a}{\partial E_\gamma} \\ &= \frac{\partial I_t}{\partial P_t} \left(\frac{\partial P_t}{\partial E_\gamma} + \frac{G_{ta,a}}{G_{ta,a}+G_{ab}} \frac{1}{1+j\omega/\omega_{ta}} \frac{\partial P_a}{\partial E_\gamma} \right) \end{aligned} \quad (11)$$

where the benefit of being able to write $\frac{\partial I_t}{\partial P_a}$ in terms of $\frac{\partial I_t}{\partial P_t}$ plus additional factors is readily apparent.

B. Noise Estimation

With the dynamical response of the detector now modeled, we can estimate the magnitude of noise from thermal power fluctuations across G_{tb} , G_{ab} , and G_{ta} , the Johnson noise across R_t and R_l and finally the first stage squid noise and compare their relative sizes by referencing them to a thermal power signal flowing directly into the TES (δP_t). This reference point was chosen purposely so that intuition from simpler 1 DOF thermal systems could be used and to suppress differences due to CRESST's use of a non-standard electronics readout scheme with a large R_l to suppress electro-thermal feedback.

With this choice of reference, thermal fluctuation noise (TFN) across G_{tb} is flat and can be estimated as

$$S_{P_t G_{tb}}(\omega) = 4k_b T_{to}^2 G_{tb} \mathcal{F}(T_{to}, T_b, \text{diffusive}) \quad (12)$$

where \mathcal{F} is a noise suppression term with a value between $\frac{1}{2}$ and 1 to account for the fact that the power noise across a thermal link between two different temperatures (a non-equilibrium situation) is less than the naively derived equilibrium noise [22]. Now, estimation of the TFN across G_{ab} is slightly more difficult since we must refer it to the TES and thus

$$\begin{aligned} S_{P_t G_{ab}} &= \left(\frac{\partial I_t}{\partial P_a} / \frac{\partial I_t}{\partial P_t} \right)^2 4k_b T_{ao}^2 G_{ab} \mathcal{F}(T_{ao}, T_b, \text{diffusive}) \\ &\sim \left(\frac{G_{ta,a}}{G_{ta,a}+G_{ab}} \right)^2 \frac{1}{1+\omega^2/\omega_{ta}^2} 4k_b T_{ao}^2 G_{ab} \mathcal{F} \end{aligned} \quad (13)$$

This noise is subdominant, even below the ω_{ta} pole since $G_{ab} \ll G_{tb}$ for both CRESST detectors (as well as for our new design).

Next, we estimate our sensitivity to thermal fluctuations between the electronic and phonon systems (i.e. across G_{ta}). We must be cognizant that these fluctuations are anti-correlated to conserve energy; if thermal power randomly flows into the phonon system, it must be flowing out of the electronic system and vice-versa. Thus, our sensitivity is

$$S_{P_t G_{ta}} = \left(\frac{\frac{\partial I_t}{\partial P_t} - \frac{\partial I_t}{\partial P_a}}{\frac{\partial I_t}{\partial P_t}} \right)^2 4k_b T_{to}^2 G_{ta} \mathcal{F}(T_{to}, T_{ao}, \text{ballistic}) \\ \sim \left(1 - \frac{G_{ta,a}}{G_{ta,a} + G_{ab}} \frac{1}{1 + j\omega/\omega_{ta}} \right)^2 4k_b T_{to}^2 G_{ta} \mathcal{F} \quad (14)$$

The insensitivity to this noise below ω_{ta} is a direct ramification of energy conservation and is a general feature of all “massless” internal thermal conductances. Of course, for the CRESST designs, this noise is again negligible compared to that from G_{tb} , simply due to their relative sizes.

TES Johnson noise is by far the most challenging to calculate for 3 reasons. One must take into account the anti-correlation between δV and δP_t [7, 22] as well as the noise boost due to current sensitivity (non-zero β) [7]. Finally, we must reference back to the TES input power. We do this in 2 steps. First, we calculate the Johnson noise referenced to current flowing through the TES (δI_t)

$$S_{I_t R_t} = \frac{4k_b T_{to} R_{to} (1 + \beta)^2}{(R_l + R_o [1 + \beta])^2} \left(1 + \frac{\partial I_t}{\partial P_t} I_{to} (R_{to} - R_l) \right)^2 \\ \sim \frac{4k_b T_{to} R_{to} (1 + \beta)^2}{(R_l + R_o [1 + \beta])^2} \left(1 - \frac{\mathcal{L}_{2D}}{\mathcal{L}_{2D} + 1} \frac{1}{1 + j\omega/\omega_{eff}} \right)^2 \quad (15)$$

where we see that the anti-correlation leads to noise suppression at low frequencies for high \mathcal{L}_{2D} . Referencing to δP_t , we obtain:

$$S_{P_t R_t} = \frac{4k_b T_{to} R_{to} (1 + \beta)^2}{(R_l + R_o [1 + \beta])^2} \left(\frac{1}{\frac{\partial I_t}{\partial P_t}} + I_{to} (R_{to} - R_l) \right)^2 \\ \sim 4k_b T_{to}^2 (G_{ta} + G_{tb}) \frac{(1 + \beta)^2}{\alpha^2 \frac{I_{to}^2 R_{to}}{(G_{ta} + G_{tb}) T_{to}}} \left(1 + \frac{j\omega}{\mathcal{L}_{2D} + 1} \right)^2 \quad (16)$$

Again, we find that as long as α is large and heating of the TES via external heating (Q) or a bath temperature (T_b) near T_c does not suppress $I_{to}^2 R_{to}$ too significantly, then the thermal fluctuations across G_{tb} dominate the noise at low frequency. However, this is clearly not true at high frequencies due to the zero at $\frac{\omega_{eff}}{\mathcal{L}_{2D} + 1}$. In fact, it is this TES Johnson noise term that sets the bandwidth for optimal energy estimators of δP_t , which we can estimate

by finding the frequency beyond which $S_{P_t R_t} > S_{P_t G_{tb}}$. This frequency, which we will designate as the signal-to-noise bandwidth, is given by:

$$\omega_{S/N \delta P_t} \sim \frac{G_{ta} + G_{tb}}{C_t} \frac{\alpha}{1 + \beta} \sqrt{\mathcal{F} \frac{G_{tb}}{G_{tb} + G_{ta}} \frac{I_{to}^2 R_{to}}{(G_{ta} + G_{tb}) T_{to}}} \quad (17)$$

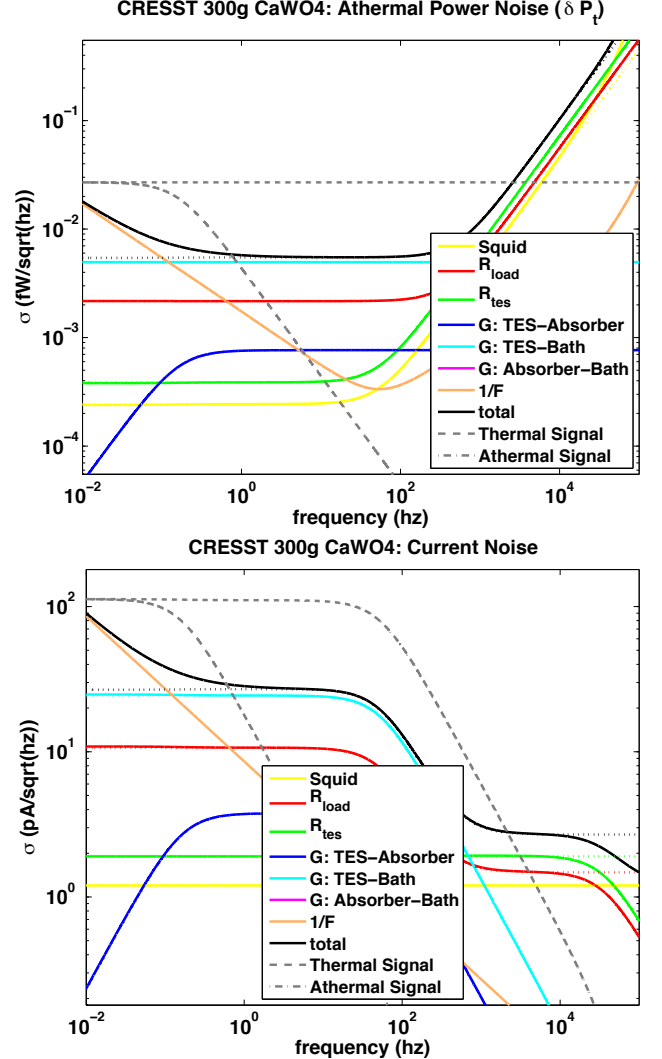


FIG. 4. Simulated noise spectrum for CRESST phonon detector referenced to TES power δP_t (top) and TES current δI_t (bottom). Dotted lines correspond to Taylor expansions in the limit of $L \rightarrow 0$ and G_{ta} & $G_{ab} \ll G_{tb}$ and no $1/f$ noise.

For electronics designs with large electro-thermal feedback, $\omega_{S/N \delta P_t} \sim \omega_{eff}$. However, for CRESST where \mathcal{L}_{2D} has purposely been set to near 0 by choosing $R_l \sim R_{to}$, $\omega_{S/N \delta P_t} \gg \omega_{eff}$. To reiterate, when referencing both the signal and noise to current (Fig. 4 bottom), both the current signal and the total current noise have a pole at ω_{eff} , and thus the signal-to-noise (which is equivalent to referencing to TES power) remains flat all the way up to $\omega_{S/N \delta P_t}$.

Unfortunately, neither the squid noise

$$S_{P_t SQUID} = \frac{1}{\frac{\partial I_t}{\partial P_t}} S_{I_t SQUID} \quad (18)$$

nor the Johnson noise from the load resistor, R_l ,

$$S_{P_t R_l} = \frac{4k_b T_{to} R_{to} (1 + \beta)^2}{(R_l + R_o [1 + \beta])^2} \left(\frac{1}{\frac{\partial I_t}{\partial P_t}} + I_{to} R_{to} (2 + \beta) \right)^2 \quad (19)$$

can be trivially written in terms of G_{tb} . However, as shown in Fig. 4 they are subdominant to the combination of G_{tb} TFN and R_t Johnson noise (this latter can also be seen through comparison of Eq. 19 to Eq. 15).

Finally, we would ideally like to have an estimate of the $1/f$ noise found in the current CRESST experimental setup, particularly since there are some indications that it could be an important contributor to the overall noise in CRESST currently [12]. More importantly, we would like to estimate the $1/f$ noise expected in a next-generation experimental setup to assess its effect on the device design. For the former, significant effort would be required that is beyond the scope of this paper. For the latter, we will use the noise performance of the SPIDER TES bolometers, which begin to be dominated by $1/f$ at 0.1 Hz, as guide to what could be achieved with effort, since CMB experiments are quite sensitive to low frequency noise [23] and thus we will set a design goal of $\omega_{S/N} \delta P_t > 0.5$ hz.

III. TES PHASE SEPARATION

Unfortunately, as first realized in the earliest days of CRESST calorimeter development [19], the simple 2 DOF block thermal model shown in Fig. 2 that we have used for our CRESST-II phonon-detector resolution estimates is not entirely accurate, since G_{tb} is also significantly larger than the internal thermal conductance of the W TES, $G_{t\text{int}}$ (cf. Table. I). In this situation, the difference in temperature between the TES T_c and the effective bath temperature is mostly internal to the TES, and thus there is a significant temperature gradient across the sensor. In devices with large α , this thermal gradient is further exasperated by positive-feedback effects of joule heating and the TES can separate into sharply defined superconducting and normal regions, with only a very thin region within the transition that is sensitive to temperature fluctuations [24].

Although a computational simulation of phase separation within the CRESST geometry is beyond the scope of this paper (and of dubious value without a very careful matching to experimental data since the dynamics depend on the resistivity of the entire transition, rather than at a single operation point), we can qualitatively discuss the ramifications.

Most importantly, a phase separated TES has significantly suppressed thermal sensitivity when biased. To

see this, we note that in the limit of $\alpha = \frac{T}{\rho} \frac{\partial \rho}{\partial T} \rightarrow \infty$ (i.e. the superconducting transition becoming infinitely sharp and infinitely sensitive to temperature variation), the DC response of the TES can be modeled analytically by tracking the fractional location of the superconducting/normal transition in the TES, x , as a function of V_b and T_b [25]. For the pertinent case where the electron-phonon coupling along the TES is negligible compared to power flow through the connection to the bath at one end of the TES, the thermal power flowing across the superconducting portion of the TES is constant and can be matched to the joule heating in the normal portion of the TES:

$$\left(\frac{V_b}{R_l + R_n x} \right)^2 R_n x = \frac{1}{1 - x} \int_{T_b}^{T_c} dT G_{t\text{int}}(T) \quad (20)$$

Using this simplification, we obtain curves of R_t versus T_b for a CRESST-like device for several values of V_b , as shown in Fig. 5.

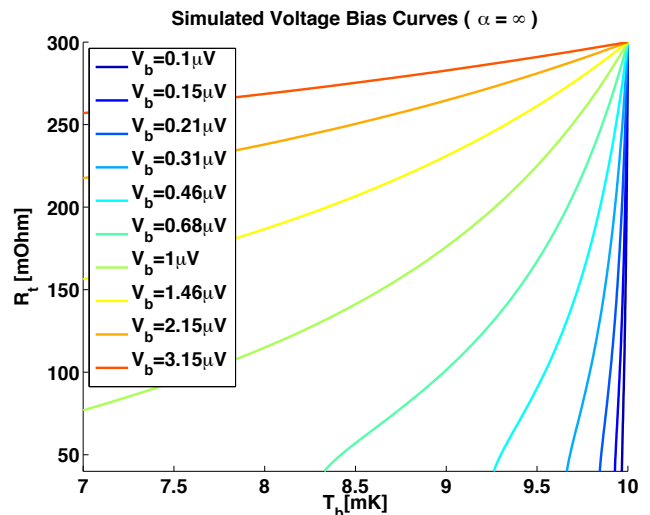


FIG. 5. Simulated R_t vs T_b curves for several values of V_b for a phase-separated TES with an infinitely sharp transition curve (at $T_c = 10$ mK) that shows DC sensitivity suppression when biased.

If not for phase separation, all of these curves would be infinitely sharp step functions centered at $T_b = T_c$. With separation though, we observe significant degradation in device sensitivity that worsens with increasing V_b . Basically, a phase separated TES acts as if it has a very large β from a DC perspective. This exact behavior is seen in CRESST devices [9, 12].

Naively, one would think that this suppression in signal amplitude would severely affect phonon power resolution at all frequency scales. However, this is not the case. At low frequencies, thermal fluctuations across G_{tb} completely dominate the noise in a non-phase-separated TES (Fig. 4 top), and thus both signal and noise are suppressed equally. Whereas at high frequencies, the total

noise is dominated by Johnson noise across the TES and thus the qualitative net effect is a suppression in $\omega_{S/N} \delta P_t$.

Further, energy that is absorbed by the TES electron system in portions of the TES that are either fully normal or superconducting must first diffuse to the transition region before producing a measurable change in current, which adds an additional strongly expressed diffusive pole into all of the TES transfer functions. In a phase separated CDMS-II TES device for example, measured $\frac{\partial I_t}{\partial V_b}$ has 2 fall-time poles (plus the R/L pole) with roughly similar weighting [26]. Beyond simply adding confusion when trying to understand and model device performance, the most important consequence is to again suppress $\omega_{S/N} \delta P_t$.

Finally, due to such large variations in the derivative of the resistivity ($\frac{\partial \rho}{\partial T}$) across the sharp superconducting/normal boundary, thermal power fluctuations within the TES directly couple to the total TES resistance R_t , and consequently the measured signal current I_t , giving us an additional noise source with fluctuations on all length scales [25]. Interestingly enough, in discretized simulations of phase separated TES for CDMS-II [26], we have found that this additional noise source is largely counter balanced by a suppression in sensitivity to standard TFN noise across G_{tb} at frequencies below the longest diffusive pole, and thus $S_{p\text{total}}$ primarily sees increases at higher frequencies.

IV. BANDWIDTH MISMATCH BETWEEN SIGNAL AND SENSOR

Before attempting to estimate the sensitivity of CRESST detectors to recoils within the absorber that have both thermal and athermal phonon components, it makes sense to calculate the expected sensitivities of the CRESST detector to the two limiting cases of a Dirac delta thermal energy deposition into the absorber and the TES. These estimates are shown in Table II.

σ_{E_e} : Eq. 1	1.0 eV
σ_{E_e} : 2D Simulated	34 eV (no 1/f) / 44 eV (1/f)
σ_{E_t} : 2D Simulated	0.5 eV (no 1/f) / 0.5 eV (1/f)
σ_{E_γ} Measured: "Julia"	420 eV [20]
σ_{E_γ} Measured: Composite	107 eV [1]

TABLE II. Simulated and measured CRESST phonon-detector energy resolutions. Note that the simulation does not include the effect of TES phase separation.

What is immediately striking is the significantly degraded expected sensitivity for thermal energy deposition in the absorber (σ_{E_a}) compared to that for direct absorption in the TES (σ_{E_t}). To understand the cause of this suppression factor, we can write σ_{E_a} in terms of σ_{E_t} under the now well motivated assumption that the noise, when referenced to δP_t , should be flat below $\omega_{S/N} \delta P_t$ (since it is dominated by the naturally flat G_{tb}):

$$\begin{aligned} \lim_{\omega_{ta} \ll \omega_{S/N} \delta P_t} \sigma_{E_a}^2 &= \frac{1}{\int_0^\infty \frac{d\omega}{2\pi} \frac{4|\frac{\partial P_t}{\partial E_a}(\omega)|^2}{S_{P_t\text{-total}}(\omega)}} \\ &\sim \frac{S_{P_t} G_{tb}(\omega=0)}{\left(\frac{G_{ta,a}}{G_{ta,a}+G_{ab}}\right)^2 \omega_{ta}} \\ &\sim \sigma_{E_t}^2 \left(\frac{G_{ta,a}+G_{ab}}{G_{ta,a}}\right)^2 \frac{\omega_{S/N} \delta P_t}{\omega_{ta}} \end{aligned} \quad (21)$$

Basically, any signal whose bandwidth is smaller than $\omega_{S/N} \delta P_t$ will suboptimally use the sensor bandwidth, leading to poorer resolution as discussed in [27]. To see this in another way, notice that both $\omega_{S/N} \delta P_t$ (Eq. 17) and $S_{p\text{total}}$ (which is roughly $S_{pt} G_{tb}$ as in Eq.12) both scale linearly with G_{tb} . Thus, as long as the bandwidth of the signal that is being measured is larger than $\omega_{S/N} \delta P_t$, the baseline energy sensitivity will be independent of the size of G_{tb} ; increasing G_{tb} increases the noise floor, but this effect is balanced by an increase in sensor bandwidth. By contrast, when measuring signals with bandwidth below $\omega_{S/N} \delta P_t$ one has accepted a noise penalty but the gained bandwidth is useless. In summary, because $\omega_{ta} \ll \omega_{S/N} \delta P_t$, the CRESST phonon detector has relatively poor sensitivity to phonon energy that is thermalized within the absorber (δP_a).

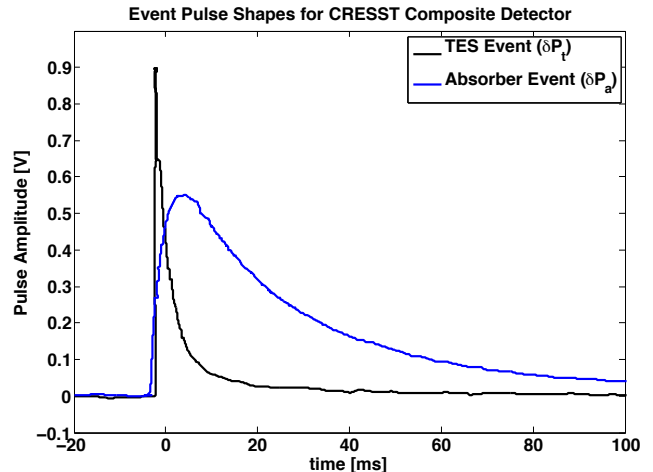


FIG. 6. Signal pulse shapes for γ -induced events in the CRESST composite detector "Rita" for events that interact in the TES chip (black) and in the absorber attached via an epoxy joint (blue). Clearly, absorber events have significantly suppressed bandwidth and consequently suppressed resolution, as in Eq. 21. Data taken from [20].

The athermal phonon signal that is thermalized in the TES bypasses the G_{ta} restriction and therefore its bandwidth is not limited by ω_{ta} . However, it still takes time to collect all of the ballistic athermal phonons rattling around in an absorber. In the SuperCDMS athermal phonon iZIP detector for example, this athermal-phonon collection bandwidth $\omega_{nt} = 210$ Hz while $\omega_{S/N} \delta P_t = 4$ kHz

for the 90 mK W TES that CDMS has historically used[26]. Thus, they pay a resolution penalty of $5\times$ due to the bandwidth mismatch between their athermal phonon signal and their sensor bandwidth, completely analogous to the thermalized sensitivity suppression.

Other examples of sensitivity suppression due to poor signal /sensor bandwidth matching can be found in the new CRESST composite detectors (Fig. 6) [20] as well as the AMORE MMC based calorimeters [28]. In the CRESST composite detector, the athermal phonon signal from an event in the absorber crystal must first be transmitted across an epoxy glue joint between the absorber crystal and the substrate on which the TES is fabricated, yielding $\omega_{nt} \sim 7$ hz (fall time ~ 23 ms). If we associate the fall-time pole of the phonon signals for events hitting the TES chip substrate (~ 50 Hz) with ω_{eff} and we further recognize that $\omega_{S/N} \delta P_t > \omega_{eff}$ for CRESST detectors (since they purposely bias to minimize electro-thermal feedback), then we can deduce that the new CRESST composite has a signal/sensor bandwidth suppression factor that is $>10\times$. In fact, using our 2D simulation, we estimate that this bandwidth-limited energy impulse into the TES, $\sigma_{E_t}(\omega_{nt} = 50$ Hz), would have a resolution of 5 eV, $10\times$ worse than the Dirac-Delta sensitivity.

In summary, our first and most important very low-temperature detector design objective is that the signal bandwidth must be larger than the sensor bandwidth, a design goal that, to our knowledge, has not been accomplished by any very low-temperature large-mass detector but that is standardly implemented in 100 mK TES calorimeters for x-ray [29] and γ [18] applications. Please note that there is some subtlety in this design rule. CRESST detectors use pulse-shape differences between absorber and TES events to suppress TES chip backgrounds (Fig. 6); they have both an energy and a discrimination signal with different bandwidths. Thus, the optimal strategy is likely to choose $\omega_{ta} \sim 1/2\omega_{S/N} \delta P_t$ so that the device discrimination threshold is equal to its energy threshold.

Secondly, if we are able to design very low-temperature calorimeters that use the entire unsuppressed sensor bandwidth (design rule 1), we will become directly sensitive to TES phase separation. Consequently we impose a second design constraint that $G_{tb} \ll G_{tint}$. As an added benefit, we think device operation and analysis will be significantly less complex, because we also naively expect that phase-separated TESs are highly sensitivity to position-dependent variations in T_c and other thin-film properties that are likely culprits for at least some of the non-linearities that have been found when biasing CRESST devices [12].

V. EXPECTED CRESST ENERGY RESOLUTION & ATHERMAL PHONON COLLECTION EFFICIENCY

We have shown that the infinite bandwidth σ_{E_t} in Table II significantly overestimates the athermal phonon energy sensitivity, since it does not account for the athermal phonon collection bandwidth, ω_{nt} . Additionally, we must account for the fact that only a fraction ϵ_{nt} of the athermal phonons are collected in the TES, and thus a particle recoil in the absorber should be modeled as

$$\begin{aligned} \frac{dP_t}{dE_\gamma} &= \frac{\epsilon_{nt}}{1 + j\omega/\omega_{nt}} \\ \frac{dP_a}{dE_\gamma} &= 1 - \epsilon_{nt} \end{aligned} \quad (22)$$

For an upper bound on ϵ_{nt} , we note that optical photons directly incident on a W TES have been measured to deposit $\sim 42\%$ of their total phonon energy into the W electronic system [30]. Another guide to the size of ϵ_{nt} comes from the SuperCDMS iZIP athermal phonon detector, which measures a total athermal phonon collection that is 10–20% of the total deposited energy [26]. Using a reasonable (but certainly not measured) value of $\epsilon_{nt} = 20\%$, we estimate a $\sigma_{E_\gamma} = 15$ eV. Although this is $7\times$ better than the best achieved resolution in a CRESST composite detector (107 eV), it is also $30\times$ worse than the naive expectation of 0.5 eV, and thus we believe that sensor/signal bandwidth mismatch and non-unity athermal phonon collection efficiency are the dominant sensitivity degradation mechanisms.

VI. PARASITIC POWER LOADING

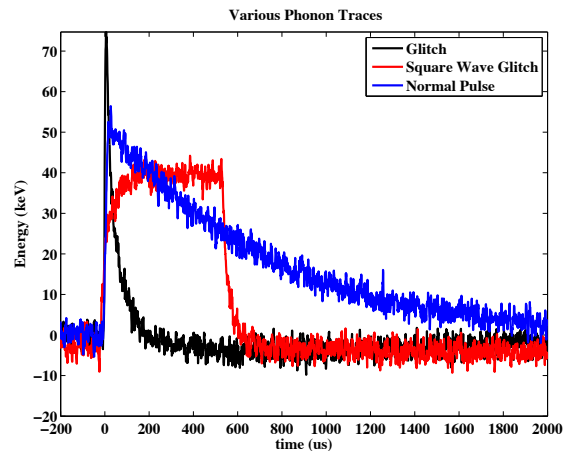


FIG. 7. Environmental noise pulses (red and black) illustrate that SuperCDMS detectors are strongly susceptible to direct TES heat by parasitic power noise.

Both design drivers so far discussed suggest that to become more sensitive an optimized very low-temperature

calorimeter should have lower G_{tb} than found in the CRESST phonon-detector design. One negative consequence of this change is greater sensitivity to parasitic heating. This is clearly a concern for SuperCDMS because their devices produce TES heating signals due to cell phone usage in the laboratory (fortunately with a very distinct pulse shape from actual events, as shown in Fig. 7), and thus the old CDMS-II electronics do not adequately shield their TESs from high-frequency environmental noise. Although this is currently only an interesting nuisance, it highlights the parasitic power problem that SuperCDMS faces. As they lower G_{tb} in their own devices, this and other parasitic power sources heat the detector to a greater and greater degree, eventually driving the TES normal and rendering it inoperable. Lower G_{tb} devices will require better environmental noise shielding.

Thus, it is reasonable to question if DC parasitic power noise necessitates the use of large G_{tb} in CRESST phonon detectors, thereby breaking our first 2 design rules and lowering detector sensitivity. Further, if so, are all very low-temperature calorimeters similarly limited? We do not believe this to be this case for 2 reasons. First, in the very same cryostat and with identical electronics, CRESST also operates light detectors that are Si or SOS wafers instrumented with the TES design shown in Fig. 8. Notice that for these detectors, the TES is not directly connected to the bath through an Au wire-bond. Instead the coupling is through a fabricated Au thin film impedance with an estimated $G_{tb} = 21.1$ pW/K for a $T_c = 10$ mK which is $350\times$ smaller than the G_{tb} of the Au wirebond used on their phonon detectors. Consequently, if DC parasitic power noise was even remotely problematic for the CRESST phonon detector, their light detector would be inoperable.

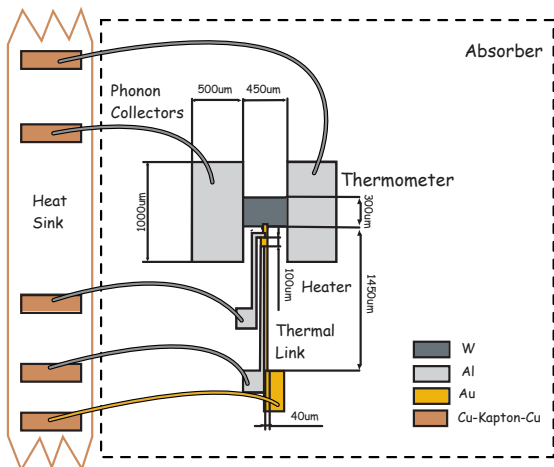


FIG. 8. TES Sensor Geometry for CRESST-II light detector [12]

Of course, when trying to assess the validity of lowering G_{tb} during the optimization of TES-based light detectors (something we also discuss due to applicability for

both dark matter and double-beta decay experiments), the above explicitly pertinent observation is insufficient. Fortunately, however, there has recently been enormous emphasis on designing TES-based sensors for space-born infrared spectrometry by SPICA/SAFARI, and they have been able to achieve parasitic power loads of ~ 2 fW, $25\times$ less than the estimated bias power, P_{to} , for the current CRESST light detector and $10^4\times$ less than their phonon detector [31]. Consequently, achieving parasitic power loads that are much less than P_{to} for low G_{tb} devices may be difficult but should be possible.

VII. LIMITS ON SENSOR BANDWIDTH DUE TO EVENT RATE

Unlike in 100 mK x-ray, γ and α calorimeters, the extremely low background and signal rates expected in underground rare-event and exotic-decay searches have meant that pileup (pulses from distinct interactions overlapping due to high rates and finite bandwidth) rejection and the ability to handle large event rates have not been primary design drivers.

In the future, however, this requirement will become much more constraining for some applications. For example, the most daunting pileup requirements come from reactor-sourced coherent neutrino scattering experiments because the cosmic background is quite large due to minimal rock overburden. As a first very rough estimate of the necessary start-time sensitivity, we note that the original CDMS shallow site experiment had a similar overburden and used an anti-coincidence window of $25 \mu\text{s}$ for activity in their plastic-scintillator muon veto [32]. Since the optimally estimated start-time resolution (assuming no pulse-shape dependence) is

$$\sigma_{t_o}^2 = \frac{1}{E^2} \frac{1}{\int_0^\infty \frac{d\omega}{2\pi} \frac{4\omega^2 \left| \frac{dI_t}{dE\gamma}(\omega) \right|^2}{S_{I_{tot}}(\omega)}} \quad (23)$$

which can be simplified to

$$\sigma_{t_o} \sim \frac{1}{\omega_{S/N} \delta P_t} \frac{\sigma_E}{E} \quad (24)$$

when flat noise is assumed and $\omega_{S/N} \delta P_t$ is the lowest pole of the design, we estimate that a reactor-sourced coherent neutrino scattering experiment needs an $\omega_{S/N} \delta P_t$ of 1.3 khz to have the requisite start-time resolution for near-threshold events ($E = 10\sigma_E$). Unfortunately, such a large $\omega_{S/N} \delta P_t$ is simply inconsistent with our other design requirements for thermal calorimeters. Consequently, we believe that this application is better suited to an athermal-only phonon detector design, as typified by a SuperCDMS detector.

Pileup rejection has also become one of the dominant design drivers for LUCIFER and other high- $Q_{\beta\beta}$ neutrinoless double-beta decay experiments because they expect the background in their signal region to be dominated by un-vetoed pileup of lower energy 2ν double-beta decay events for which pileup rejection is assumed to

be ineffectual below 5 ms [10]. Luckily, with such a large signal, start-time resolutions of this order are achievable (see Sec. X) and thus, if required, this is a reasonable design requirement.

VIII. EASE OF FABRICATION & COSMOGENIC BACKGROUND SUPPRESSION: SEPARATED TES CHIP

CUORE and EDELWEISS have continued to use NTD sensor technology, despite the many benefits offered by TES readout, including:

1. A TES is fundamentally more sensitive than a NTD (larger α);
2. The SQUIDS used in TES readout have lower $1/f$ noise than JFETs or HEMTs used for first stage amplification for NTDs;
3. Low-impedance sensors (TESs) are fundamentally less sensitive to vibrationally induced capacitance changes in readout compared to high-impedance sensors (NTDs); and
4. SQUIDS have significantly lower heat loads than the JFETs or HEMTs used in NTD readout, and can therefore be placed significantly closer to the detector, simplifying electronics and cryostat design.

One reason for this is that both TES-based massive-detector groups (CRESST and CDMS) fabricated their TESs directly upon the absorber surface, a feat that required enormous fabrication process R&D since every facet of standard microprocessor fabrication (photolithography, etching, thin film deposition) had to be retrofitted for thick and massive substrates. In fact, even with over a decade of R&D, fabrication yields were still a significant resource drain until recently on CDMS. Further, the time and labor intensive nature of microprocessing fabrication means that absorbers spend a significant amount of time on the surface being cosmogenically activated, certainly a disadvantage for low mass WIMP searches, for example. This direct absorber fabrication is required since the W TES in CRESST has 2 distinct functions. First, it is a temperature sensor. This is the functionality that requires microprocessor fabrication techniques on multiple different thin film layers: Al for the superconducting bias rails, W for the TES, and Au for the thermal connection to bath. Second, the electron-phonon coupling within the W film acts as G_{ta} . Because it is only this latter functionality that requires fabrication directly upon the absorber, design goals of fabrication simplicity and minimum cosmogenic exposure require that the TES does not act as the thermal link between the sensor and the absorber.

As illustrated in Fig. 9, we propose to deposit a large, single layer Au thin-film pad directly onto the large absorber substrates that plays the role of G_{ta} . This can

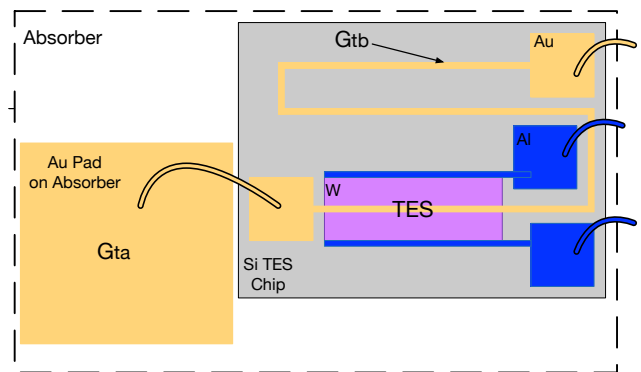


FIG. 9. Optimized large-mass calorimeter sensor design. Only the large Au pad is directly fabricated on the large absorber.

be done using only shadow mask techniques (albeit with a deposition machine modified for thick substrates) and consequently fabrication should have very high yield and be relatively hassle free since there is no photolithography and etching. As an added benefit (in fact, perhaps the most important benefit), this permits use of any metal rather than being constrained to W; we choose Au which has an order of magnitude larger electron-phonon coupling than W for a given thermal capacitance.

The fabrication intensive TES can then be separately fabricated on standard thin substrates for fabrication ease, where the material chosen is not necessarily identical to that of the large absorber (Si, Ge, Al_2O_3 , CaWO_4). Further, each and every 100 mm wafer can produce over 20 devices. Thus, device fabrication throughput could easily be $80\times$ that of CDMS (in the standard SuperCDMS fabrication procedure, 4 fully processed test wafers are produced for every detector). This physical separation also allows for testing of the TES sensor die above ground before connection to the absorber. This has significant advantages: the cost savings of sensor testing above ground rather than in an underground laboratory is substantial; and one can choose only the best sensors to match with expensive absorbers, particularly useful in the case of double-beta decay enriched crystals.

Thermal connection between the TES and the G_{ta} absorber pad is then accomplished via Au wire bonding, while the simpler mechanical connection can be accomplished with epoxy in an arbitrary (and somewhat haphazard) manner; without any thermal-conductance requirements, very small-area single dot epoxy joints are possible that do not mechanically stress the absorber [20]). Another possibility is that the TES chips are mechanically supported by the detector housing. Of course, the heat capacity of the Au wirebond between the TES and the absorber (~ 1 pJ/K at 10 mK) is entirely parasitic and is simply the price paid for the ease of fabrication. Most importantly, the thermal conductance of both the internal pad, $G_{pad\ int}$, and that of the Au wirebond, $G_{bond\ int}$, must be much larger than G_{tb} so as to satisfy the bandwidth design rules discussed in Sec. IV.

It is interesting to reiterate how similar and yet how distinct this design is from the CRESST composite detector [20]. On the one hand, this design is clearly derivative. As with the CRESST composite detector, the TES is fabricated on a separate and much thinner substrate that drastically simplifies fabrication (and in the CRESST case, improves scintillation yield in the primary absorber). On the other hand, the difference is profound. In the CRESST design, energy transport between the 2 systems is accomplished via phonon transport through an epoxy joint that significantly suppresses both athermal and thermal signal bandwidths (making our bandwidth design objectives very difficult to achieve). Further, low-impedance phonon transport via epoxy couplings requires large cross-sectional areas that make the detector much more prone to crack via differential thermal contraction among the epoxy, the absorber substrate, and the TES chip substrate. The CRESST composite detector mitigates this problem somewhat by using CaWO_4 for both the TES substrate and the absorber. However, this limits possible detector materials. NaI, for example, is an attractive material to search for spin or orbital angular momentum coupling dark matter [33]. Furthermore, scintillating NaI calorimeters would directly test the anomalous annual modulation signal observed in DAMA [34]. Unfortunately though, NaI is very hygroscopic and thus any complex photolithography is impossible.

In summary, this design should retain all the benefits of TES performance and yet also have the fabrication simplicity, cosmogenic benefits, and material freedom of NTD based detectors.

This device design should also be critically compared to the AMORE MMC calorimeter design [28]. Removing the trivial difference of the use of an MMC instead of a TES sensor element, all pertinent design rules that we have developed were followed with the single and very important exception that their sensor bandwidth is much larger than their signal bandwidth (ω_{ta}). This choice suppresses their zero energy sensitivity but even more importantly drastically increases their sensitivity to position dependence (Secs. IX and X), a fact that severely limits the viability of their current devices.

IX. POSITION DEPENDENCE REQUIREMENTS IN NEUTRINOLESS DOUBLE BETA DECAY SEARCHES

Because of the approximately exponential shape of the WIMP nuclear-recoil energy spectrum, a slight position or temporal systematic of $<5\%$ on the recoil energy estimate in a CRESST phonon detector does not significantly affect their sensitivity. By contrast, a neutrinoless double-beta decay experiment like CUORE/LUCIFER [10] requires the maximum achievable energy resolution at 3 MeV , and thus any variation in the pulse shape or magnitude of the signal due to event location in the ab-

sorber must be minimized in addition to having excellent baseline energy sensitivity. Specifically, a well designed double beta detector should be limited by systematics in the absorber thermalization process, with $\frac{\Delta E}{E}$ measured to be 5×10^{-4} in TeO_2 [35]) and 2×10^{-3} in ZnMoO_4 [10].

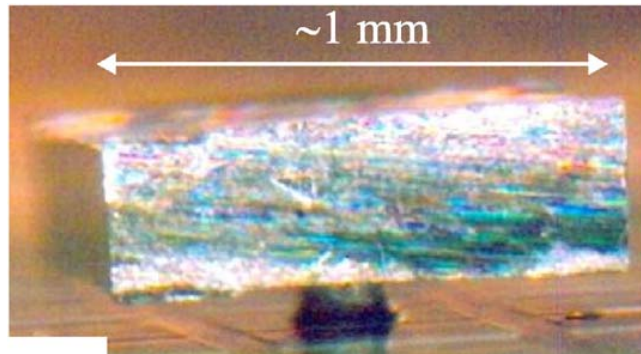


FIG. 10. NIST γ calorimeter with $\sigma = 21\text{ eV}$ at 103 keV using a TES with $T_c \sim 100\text{ mK}$. [18]

To guide us in developing design rules to minimize position dependence, let us look more carefully at the 100 mK TES γ calorimeter shown in Fig. 10 that achieved a $\frac{\Delta E}{E} < 5 \times 10^{-4}$ [18]. First and foremost, the only thermal and structural link between the absorber and the bath goes through the TES ($G_{ab}=0$). To illustrate the importance of this for suppressing position dependence, consider the design in [11] where the primary thermal path from the TES to the bath is through the absorber ($G_{tb} = 0, G_{ab} \neq 0$). In this case, athermal phonons produced in the initial interaction will preferentially thermalize in either the TES (G_{tb}) or in the metal pad thermally linked to the bath (G_{ab}), depending on the event's location in the absorber and leading to significant unwanted position dependence in δI_t .

Unfortunately, G_{ab} free designs are significantly more difficult to achieve when the absorber weighs $\mathcal{O}(kg)$ rather than $\mathcal{O}(g)$, and thus this will be an aspirational goal rather than a requirement. We will solely require that $G_{ab} \ll G_{ta}$, and that any G_{ab} be diffusive rather than ballistic so that non-thermalized excitations would find it difficult to escape through G_{ab} .

Secondly, the size of the diffusive-phonon thermal link between the absorber and the TES in this γ calorimeter was chosen to be much slower than the thermalization/position-dependent time scale, $\omega_{nt} \gg \omega_{ta} \gg \omega_{S/N} \delta P_t$. This choice means that unwanted position information with frequencies around ω_{nt} have 2 pole suppression over many decades in their current response.

Unfortunately, thermalization is very slow in the insulator and semiconductor absorbers used in massive calorimeters compared to the superconductors and metal absorbers used in γ and x-ray calorimeters. SuperCDMS iZIP detectors, for example, see variations in athermal phonon power absorbed by different channels on the same crystal up to $300\ \mu\text{s}$ after an event interaction. Such long position-dependent thermalization times put downward

pressure on both ω_{ta} and $\omega_{S/N \delta P_t}$ when using this bandwidth design scheme. CUORE actually attempts to do exactly this in their NTD based calorimeter by using a small dot of epoxy as G_{ta} , with the hope of suppressing any non-thermalized position-dependent phonon signal from reaching their TES. Unfortunately, this choice in combination with poor electron-phonon coupling within the NTD means that $G_{ab} > G_{ta}$, and thus most of the absorbed energy is not measured by the NTD but directly shunted to the bath, suppressing baseline energy sensitivity and increasing DC susceptibility to position dependence [21].

In our proposed calorimeter design, the above bandwidth design scheme is very difficult to achieve because the dominant phonon thermalization mechanism is through electron-phonon coupling within the metal pad that acts as G_{ta} ; $\frac{\partial P_t}{\partial E_\gamma}$ (Eq. 11) will always be non-zero. Thus, we must be content with single-pole suppression of position dependence. On the otherhand, since we now control the rate of athermal phonon thermalization (ω_{nt}), we can maximize this single-pole suppression by making the pad as large as possible (i.e. set the design requirement that $\omega_{nt} \& \omega_{ta} \gg \omega_{S/N \delta P_t}$). As an aside, note that suppression of position dependence via pole suppression is incompatible with the pulse-shape discrimination between TES chip events and absorber events that CRESST enjoys because it requires ($\omega_{ta} \sim \frac{1}{2} \omega_{S/N \delta P_t}$).

As a rough but conservative estimate of the position-dependent systematics in both the energy and start-time estimators, we assume that the thermal power signals into the TES and absorber can be modeled as

$$\begin{aligned} \frac{dP_t}{dE_\gamma} &= \epsilon \\ \frac{dP_a}{dE_\gamma} &= 1 - \epsilon \end{aligned} \quad (25)$$

where we vary ϵ from 0–10%, using SuperCDMS position dependence as a rough guide (we have pushed $\omega_{nt} \rightarrow \infty$ to maximally accentuate the position dependencies).

X. DESIGN SKETCH OF 1.75KG ZnMoO_4 DETECTOR FOR NEUTRINOLESS DOUBLE BETA DECAY

In Table. III we flesh out the specifications and simulated performance for a 1.75 kg ZnMoO_4 device that follows all of the design rules so far discussed. Such a massive absorber (or the addition of parasitic heat capacitance as was done in [6]) is required to keep $Q_{\beta\beta}$ within the dynamic range of the TES. We recognize that the use of such large crystals increases the need for pileup rejection (i.e. timing requirements) [10].

The Au pad volume on the absorber was chosen to be quite large so that $\omega_{ta} \gg \omega_{S/N \delta P_t}$. Notice that even with such a relatively large volume, the parasitic heat capacity of the pad is only $\sim 80\%$ that of the ZnMoO_4 . The

ZnMoO ₄ absorber			
V_a	Volume		$\pi(40\text{mm})^2 \times 80\text{mm}$
T_{ao}	Operational temperature		9.33 mK
C_a	Heat capacity	$\Gamma_{\text{ZnMoO}_4} V_a T_{ao}^3$	191 $\frac{\text{pJ}}{\text{K}}$
Au thin film thermal link between TES and bath			
l_{tb}	Length		900 μm
A_{tb}	Cross sectional area		10 $\mu\text{m} \times 300 \text{ nm}$
G_{tb}	Thermal conductance from TES to bath	$\frac{v_f d_e}{3} \Gamma_{Au} T_{to} \frac{A_{tb}}{l_{tb}}$	286 $\frac{\text{pW}}{\text{K}}$
Au thermalization film on absorber (p1)			
V_{p1}	Volume		$4\pi(9\text{mm})^2 \times 300\text{nm}$
$C_{t p1}$	p1 component of TES heat capacity	$\Gamma_{Au} V_{p1} T_{to}$	187 $\frac{\text{pJ}}{\text{K}}$
G_{ta}	Thermal conductance between TES and absorber	$n_{ep} \Sigma_{ep} V_{p1} T_{to}^{n_{ep}-1}$	37 $\frac{\text{nW}}{\text{K}}$
Au wirebond between TES and absorber			
l_w	Length		1.0 cm
A_w	Cross sectional area		$4\pi(7.5\mu\text{m})^2$
G_w	Thermal conductance	$\frac{v_f d_e}{3} \gamma_{Au} T_{to} \frac{A_w}{l_w}$	21.6 $\frac{\text{nW}}{\text{K}}$
$C_{t w}$	Bond component of TES heat capacity		4.6 $\frac{\text{pJ}}{\text{K}}$
W TES			
A_t	Cross sectional area		3.5 mmx150 nm
l_t	Length		700 μm
T_c	Transition temperature		10 mK
ΔT_{90-10}	Transition width	$(T_{90\%}-T_{10\%})$	2 mK
T_{to}	Operating temperature		9.33 mK
I_{to}	Operating current		5.4 μA
$C_{t w}$	W component of TES heat capacity	$f_{sc} \Gamma_w V_t T_{to}$	0.96 $\frac{\text{pJ}}{\text{K}}$
$G_{t int}$	Internal TES conductance	$\frac{L_w f}{\rho_w} \frac{A_t}{l_t/2} T_{to}$	4.9 $\frac{\text{nW}}{\text{K}}$
R_n	Normal resistance	$\rho_w \frac{l_t}{A_t}$	100 $m\Omega$
R_{to}	Operating point	$R_n/5$	20 $m\Omega$
α	Thermal sensitivity	$\left. \frac{T_{to}}{R_{to}} \frac{\partial R}{\partial T} \right _{I_{to}}$	16.4
β	Current sensitivity	$\left. \frac{I_{to}}{R_{to}} \frac{\partial R}{\partial I} \right _{T_{to}}$	0.05
Dynamical time constants			
$\tau_{L/R}$	Squid inductor time constant		15 μs
τ_{eff}	sensor fall time		365 ms
τ_{ta}	Absorber/TES coupling time constant		2.6 ms
Estimated resolution and saturation energy			
σ_E	Estimated baseline energy resolution		3.54 eV
σ_{to}	Estimated timing resolution @ 3 MeV		170 μs
$\Delta E/E$	Position dependence		6×10^{-4}
E_{sat}	Absorber saturation energy		4.1 MeV

TABLE III. Optimized 1.75kg ZnMoO_4 detector for next-generation double-beta decay experiments

thickness of the pad at 300 nm was a compromise. On the one hand we wanted to cover the the largest possible surface area, so as to maximize ω_{nt} . On the otherhand, we want the internal thermal conduction of the pad $G_{pad\,int} \gg G_{ta}$. Since the parasitic heat capacity of an individual Au wire bond is also relatively small (1.2 pJ/K) compared to the crystal, we used 4 and assumed an extra long 200 μm bond tail at both ends for greater thermal conductance.

For the TES itself, we chose a W TES with an $R_n=100\text{ m}\Omega$ that we would run low in the transition (20% R_n) to maximize the dynamic range. Further, we would use $R_l=3\text{ m}\Omega$ to be in the strong electro-thermal limit. This aspect ratio was chosen so that $G_{t\,int} \gg G_{tb}$ and could potentially be further lowered. Since the heat capacity of the TES is subdominant compared to both the crystal and the G_{ta} pad, the sole constraints on its size are related to sensor performance related. Since β increases with current density (which scales as $V_t^{-1/2}$, where V_t is the TES volume), we will choose the overall TES size such that the current density is 1/2 that found in the current CRESST detectors. The use of low-resistivity Ir/Au or Mo/Au bilayers [19, 36, 37] is also certainly possible and would suppress TES inhomogeneities but with the potential for larger β .

Finally, G_{tb} , is a thin Au film impedance similar to that used by CRESST in their original light detectors [12]. Its size is set so that $\omega_{S/N} \delta P_t$ is as small as allowed by 1/f noise constraints.

The simulated baseline energy resolution of 3.54 eV is clearly sufficient for double beta decay (Simulated Noise PSDs in Fig. 11). For a rough estimate of the position sensitivity, we have simulated position-dependent pulse shapes for $\epsilon = 0, 5,$ and 10% (Eq. 25, Fig. 12), and using the standard optimum sensitivity estimator we estimate a $\frac{\Delta E}{E}$ of 6×10^{-4} which is just adequate for current purity TeO_2 and ZnMoO_4 . Further, SuperCDMS has been able to suppress unwanted position dependence in their phonon energy estimators by an additional factor of 2–4 using non-stationary optimum filters or multiple template optimum filters. Techniques such as these could be even more viable for double-beta decay detectors since the residual dependence in SuperCDMS is due largely to variations in Luke phonon production due to ionized e^- trapping [26].

This slight sensitivity to athermal phonons that systematically biases our energy estimator does have one hidden silver lining: our devices should have significantly improved timing and pulse-shape rejection from the largely decoupled NTDs currently used by CUORE/LUCIFER, a significant advantage. We find that position-dependent systematics dominate our start-time sensitivity and limit our start-time resolution to 170 μs ($\sigma_{t_o} = 50\ \mu\text{s}$ if noise limited).

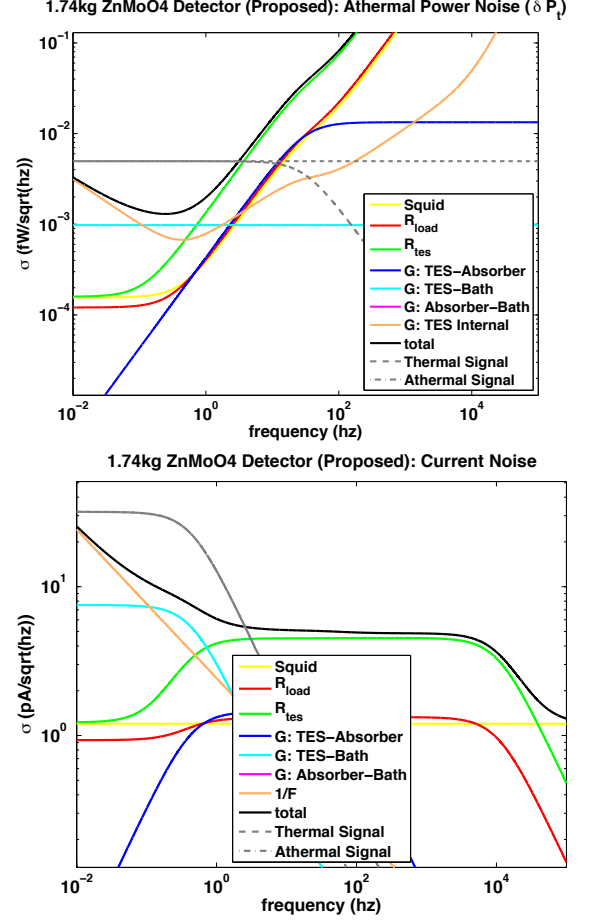


FIG. 11. Simulated noise referenced to TES power (top) and current (bottom) for a 1.74kg ZnMoO_4 detector.

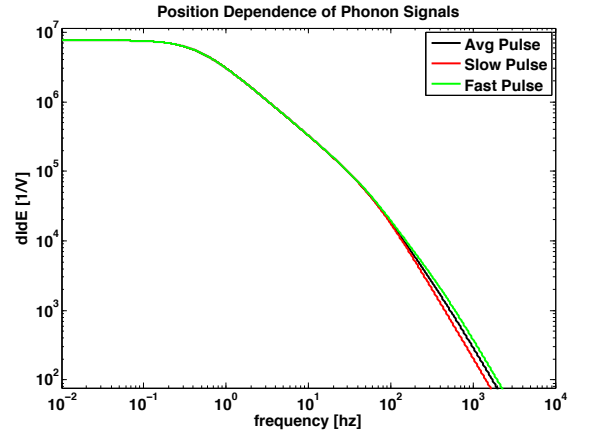


FIG. 12. Simulated pulse shapes for events from different locations in the absorber for a 1.74 kg ZnMoO_4 detector.

XI. SINGLE PHOTON LIGHT DETECTOR

These very same design rules can also be applied to (hopefully) significantly improve the performance of very low-temperature, large-area light detectors which are

used to distinguish electronic recoils from nuclear recoils for both dark matter and double-beta decay detectors. For CRESST, a single-photon sensitive detector would be very beneficial because their low-mass WIMP sensitivity is suppressed by electron-recoil backgrounds leaking into the WIMP signal region [1], while for double-beta decay experiments, single-photon sensitivity could potentially be used for electron/nuclear-recoil discrimination in non-scintillating crystals like TeO_2 via Cherenkov light collection [38].

The $30 \text{ mm} \times 30 \text{ mm}$ Si chip used in the original CRESST light detectors has a phonon heat capacity of only 220 fJ/K at 10 mK , and consequently the parasitic heat capacity of the Au wirebond between the Si TES chip and the large Si wafer (unfortunately) totally dominates the overall sensor heat capacity as outlined in Table IV. On the brightside, this allows us to increase the size of the Si chip to 80 mm diameter, thereby improving the scintillation collection efficiency without significant loss of energy sensitivity. The Au thin-film meander which thermally connects the TES to the bath was chosen so that $\tau_{\text{eff}} \sim 50 \text{ ms}$, long enough to be minimally sensitive to both the precise location of the scintillation absorption in the Si and to stochastic fluctuations in the scintillation creation/absorption time ($O(1 \text{ ms})$ in many crystals), yet small enough to retain significant start-time information that could be vital for application of this technology to double-beta decay with ZnMoO_4 crystals[10]. Specifically, the expected noise-limited optimal-filter start-time resolution for a $\sim 1.5 \text{ keV}$ scintillation signal accompanying a 3 MeV electron recoil in ZnMoO_4 is found to be $2.2 \mu\text{s}$ (assuming instantaneous photon release/capture). Clearly, this is a drastic underestimate for slowly scintillating crystals, but it suggests that pileup rejection with the photon detector could be viable in fast scintillating crystals.

The expected energy-resolution performance of 0.36 eV is well below the single-photon quanta energy of $\sim 2 \text{ eV}$ for most scintillating crystals, and consequently this device can be characterized as a highly efficient large-area single-photon detector. If additional sensitivity is required, the TES could be directly fabricated onto the Si chip for improved performance. Of course, one would then lose the fabrication rate benefit of being able to make ~ 20 devices per wafer. On the other hand, Si wafer processing is standard.

XII. CONCLUSIONS

The small heat capacitance of insulating and semiconducting crystals at very low temperatures suggests that eV-scale energy resolution is possible in massive, kilogram thermal detectors operating around 10 mK . Unfortunately, with achieved sensitivities 2–3 orders of magnitude worse than these expectations, the current generation of detectors have yet to fully realize this potential. The dominant culprit for this discrepancy is

Si absorber			
V_a	Volume		$\pi(4 \text{ cm})^2 \times 525 \mu\text{m}$
M_a	Mass		6.0 g
T_{ao}	Operation temperature		9.3 mK
C_a	Heat capacity	$\Gamma_{Si} V_a T_{ao}^3$	$1.6 \frac{\text{pJ}}{\text{K}}$
Au thin film thermal link between TES and bath			
l_{tb}	Length		6.0 mm
A_{tb}	Cross sectional area		$5 \mu\text{m} \times 300 \text{ nm}$
G_{tb}	Thermal conductance from TES to bath	$\frac{\nu_f d_e}{3} \Gamma_{Au} T_{to} \frac{A_{tb}}{l_{tb}}$	$23 \frac{\text{pW}}{\text{K}}$
Au thermalization film on absorber (p1)			
V_{p1}	volume		$\pi(3 \text{ mm})^2 \times 100 \text{ nm}$
$C_{t p1}$	p1 component of TES heat capacity	$\gamma_{Au} V_{p1} T_{to}$	$1.9 \frac{\text{pJ}}{\text{K}}$
G_{ta}	Thermal conductance between TES and absorber	$n_{ep} \Sigma_{ep} V_{p1} T_{to}^{n_{ep}-1}$	$452 \frac{\text{pW}}{\text{K}}$
Au wirebond between TES and absorber			
l_w	length		1.0 cm
A_w	Cross sectional area		$\pi(7.5 \mu\text{m})^2$
G_w	Thermal conductance	$\frac{\nu_f d_e}{3} \Gamma_{Au} T_{to} \frac{A_w}{l_w}$	$5.4 \frac{\text{nW}}{\text{K}}$
$C_{t w}$	Bond component of TES heat capacity		$1.16 \frac{\text{pJ}}{\text{K}}$
W TES			
A_t	Cross sectional area		$1520 \mu\text{m} \times 150 \text{ nm}$
l_t	Length		$300 \mu\text{m}$
T_c	Transition temperature		10 mK
I_{to}	Operating current		$1.48 \mu\text{A}$
T_{to}	Operating temperature		9.3 mK
$G_{t int}$	Internal TES conductance	$\frac{L_w f}{\rho W} \frac{A_t}{l_t/2} T_{to}$	$4.9 \frac{\text{nW}}{\text{K}}$
$C_{t w}$	W component of TES heat capacity	$f_{sc} \Gamma_W V_t T_{to}$	$0.18 \frac{\text{pJ}}{\text{K}}$
R_n	Normal resistance	$\rho W \frac{l_t}{A_t}$	100 $m\Omega$
R_{to}	Operating resistance	$R_n/4$	20 $m\Omega$
α	Thermal sensitivity	$\left. \frac{T_{to}}{R_{to}} \frac{\partial R}{\partial T} \right _{T_{to}}$	16.4
β	Current sensitivity	$\left. \frac{I_{to}}{R_{to}} \frac{\partial R}{\partial I} \right _{T_{to}}$	0.03
Dynamical time constants			
$\tau_{L/R}$	Squid Inductor Time Constant		15 μs
τ_{eff}	Sensor Fall Time		56ms
τ_{sa}	Absorber/ TES Coupling Time Constant		2.6ms
Estimated Resolution			
σ_E	Estimated Baseline Energy Resolution		0.36eV
σ_{to}	Estimated Timing Resolution @ 1.5keV		2.2 μs

TABLE IV. Optimized Light Detector

that electron-phonon coupling in both TESs and NTDs drops rapidly with temperature, and thus the electron system within the sensor decouples from the phonon system within the absorber leading to the absorber phonon signal bandwidth being much smaller than the sensor bandwidth and/or shunting of the signal past the sensor through parasitic thermal conductance channels.

After a detailed study of current-generation detectors, we developed prototype designs for both an 80 mm diameter Si light detector and a 1.75 kg ZnMoO₄ massive calorimeter for which the sensor bandwidth is smaller than the signal bandwidth yet still larger than an expected $1/f$ noise threshold as well as the bandwidth requirements due to event rate. Consequently, we estimate device sensitivities of 0.4 eV and 3.4 eV that nearly match the expected scaling law performance. Further, we have shown that these lower G_{tb} designs have achievable parasitic power requirements via comparison to detectors made by SPICA/SAFARI for infrared spectrometry applications.

Additionally, for fabrication simplicity and suppression of cosmogenic backgrounds, both of these designs use a single layer Au thin-film pad that is deposited directly onto the absorber (using simple shadow mask techniques) for electron-phonon coupling rather than fabricating the entire TES onto the absorber. This pad is then thermally

connected via an Au wirebond to a separately fabricated TES chip.

Finally, we have shown that position systematics on energy estimators can still be suppressed to the level that they are subdominant compared to thermalization systematics in both TeO₂ and ZnMoO₄ crystals. This is achieved despite purposely designing our detector to have large coupling between the electronic system within the TES and the phonon system in the absorber by requiring that the sensor bandwidth be smaller than the athermal phonon collection bandwidth.

XIII. ACKNOWLEDGEMENTS

The authors would like to thank Ray Bunker, Blas Cabrera, Raul Hennings-Yeomans, Kent Irwin, Alexandre Juillard, Yury Kolomensky, Nader Mirabolfathi, Wolfgang Rau, and Philippe Di Stefano for interesting and insightful discussions and comments.

Appendix A: Pertinent Material Properties

-
- [1] G. Angloher *et al.* (CRESST-II Collaboration), (2014), arXiv:1407.3146 [astro-ph.CO].
 - [2] C. Arnaboldi and et al, Physical Review C **78** (2008).
 - [3] E. Armengaud and et al (EDELWEISS-II), Physics Letters B **702**, 329 (2011).
 - [4] Z. Ahmed and et al (CDMS II), Science **327**, 1619 (2010).
 - [5] A. E. Lita, A. J. Miller, and S. W. Nam, Optics Express **16**, 3032 (2008).
 - [6] R. D. Horansky and et al, Applied Physics Letters **93** (2008).
 - [7] K. Irwin and G. Hilton, Topics in Applied Physics **99** (2005).
 - [8] G. Angloher and et al, Astroparticle Physics **31**, 270 (2009).
 - [9] M. Sisti and et al, Nuclear Instruments and Methods A **466**, 499 (2001).
 - [10] The European Physical Journal C **72**, 2142 (2012).
 - [11] J. A. Formaggio and E. Figueroa-Feliciano, Physical Review D **85** (2012).
 - [12] E. Pantic, *Performance of Cryogenic Light detectors in the CRESST-II Dark Matter Search*, Ph.D. thesis, Technische Universitat Munchen (2008).
 - [13] G. Angloher and et al, Astroparticle Physics **23**, 325 (2005).
 - [14] S. Henry, N. Bazin, H. Kraus, B. Majorovits, M. Malek, R. McGowan, V. B. Mikhailik, Y. Ramachers, and A. J. B. Tolhurst, Journal of Instrumentation **2**, P11003 (2007).
 - [15] E. Figueroa-Feliciano, *Theory and Development of Position-Sensitive Quantum Calorimeters*, Ph.D. thesis, Stanford University (2001).
 - [16] E. Figueroa-Feliciano, Journal of Applied Physics **99**, 114513 (2006).
 - [17] S. J. Smith, S. R. Bandler, R. P. Brekosky, A.-D. Brown, J. A. Chervenak, M. E. Eckart, E. Figueroa-Feliciano, F. M. Finkbeiner, R. L. Kelley, C. A. Kilbourne, F. S. Porter, and J. E. Sadleir, IEEE Transactions on Applied Superconductivity **19**, 451 (2009).
 - [18] B. L. Zink, J. N. Ullom, J. A. Beall, K. D. Irwin, W. B. Doriese, W. D. Duncan, L. Ferreira, G. C. Hilton, R. D. Horansky, C. D. Reintsema, and L. R. Vale, Applied Physics Letters **89**, 124101 (2006).
 - [19] F. Probst and et al, Journal of Low Temperature Physics **100**, 69 (1995).
 - [20] M. Kiefer *et al.* (CRESST-II Collaboration), (2009), arXiv:0912.0170 [astro-ph.CO].
 - [21] A. Alessandrello, C. Brofferio, D. Camin, O. Cremonesi, A. Giuliani, M. Pavan, G. Pessina, and E. Previtali, in *Nuclear Science Symposium and Medical Imaging Conference, 1992.*, *Conference Record of the 1992 IEEE* (1992) pp. 98–100 vol.1.
 - [22] McCammon, Topics in Applied Physics **99** (2005).
 - [23] J. Bonetti, P. Day, M. Kenyon, C.-L. Kuo, A. Turner, H. Leduc, and J. Bock, Applied Superconductivity, IEEE Transactions on **19**, 520 (2009).
 - [24] B. Cabrera, NIM A **44**, 304 (2000).
 - [25] A. Luukanen and et al, Physical Review Letters **90**, 238306 (2003).
 - [26] M. Pyle, *Optimizing the Design and Analysis of Cryogenic Semiconductor Dark Matter Detectors for Maximum Sensitivity*, Ph.D. thesis, Stanford University (2012).

Tungsten Properties		
Γ_W	electronic heat capacity coefficient	$107 \frac{J}{m^3 K^2}$ [39]
n_{ep}	electron-phonon thermal power exponent	5 [40]
Σ_{epW}	electron-phonon coupling coefficient	$0.32 \times 10^9 \frac{W}{m^3 K^5}$ [40]
ρ_W	W electrical resistivity	$7.6 \times 10^{-8} \Omega m$ [13]
f_{sc}	superconductor/normal metal heat capacity ratio	2.54
Gold Properties		
Γ_{Au}	electronic heat capacity coefficient	$66 \frac{J}{m^3 K^2}$ [41]
n_{eAu}	free electron density	$5.90 \times 10^{28} \frac{1}{m^3}$ [41]
v_{fAu}	fermi velocity	$1.4 \times 10^6 \frac{m}{s}$ [41]
d_{eAu}	electron diffusion length (not annealed)	$\min(1 \mu m, \text{thickness})$ [42]
n_{ep}	electron-phonon thermal power exponent	5
Σ_{epAu}	electron-phonon coupling coefficient	$3.2 \times 10^9 \frac{W}{m^3 K^5}$
Silicon Properties		
ρ_{nSi}	atomic number density	$5.00 \times 10^{28} \frac{1}{m^3}$
T_{DSi}	Debye temperature	645K [43]
Γ_{Si}	phonon heat capacity coefficient: $\frac{12\pi^4 k_b \rho_{nSi}}{5T_{DSi}^3}$	$0.6025 \frac{J}{m^3 K^4}$
CaWO ₄ Properties		
$\rho_{n,CaWO_4}$	unit cell number density	$1.267 \times 10^{28} \frac{1}{m^3}$
$T_{D,CaWO_4}$	Debye temperature	250K [44]
Γ_{CaWO_4}	phonon heat capacity coefficient: $\frac{12\pi^4 k_b \rho_{n,CaWO_4}}{5T_{D,CaWO_4}^3}$	$2.6182 \frac{J}{m^3 K^4}$
ZnMoO ₄ Properties		
$\rho_{n,ZnMoO_4}$	unit cell number density	$1.267 \times 10^{28} \frac{1}{m^3}$
$T_{D,ZnMoO_4}$	Debye temperature	250K [44]
Γ_{ZnMoO_4}	phonon heat capacity coefficient: $\frac{12\pi^4 k_b \rho_{n,ZnMoO_4}}{5T_{D,ZnMoO_4}^3}$	$2.6182 \frac{J}{m^3 K^4}$

TABLE V. Pertinent Material Properties

[27] B. Sadoulet, Nuclear Instruments and Methods in Physics Research Section A: Accelerators, Spectrometers, Detectors and Associated Equipment **370**, 61 (1996), proceedings of the Sixth International Workshop on Low Temperature Detectors.

[28] G. Kim, S. Choi, Y. Jang, H. Kim, Y. Kim, V. Kobychyev, H. Lee, J. Lee, J. Lee, M. Lee, S. Lee, and W. Yoon, Journal of Low Temperature Physics **176**, 637 (2014).

[29] T. Saab, S. R. Bandler, K. Boyce, J. A. Chervenak, E. FigueroaFeliciano, N. Iyomoto, R. L. Kelley, C. A. Kilbourne, F. S. Porter, and J. E. Sadleir, AIP Confer-

ence Proceedings **850**, 1605 (2006).

[30] J. Burney, T. Bay, J. Barral, P. Brink, B. Cabrera, J. Castle, A. Miller, S. Nam, D. Rosenberg, R. Romani, and A. Tomada, Nuclear Instruments and Methods in Physics Research Section A: Accelerators, Spectrometers, Detectors and Associated Equipment **559**, 525 (2006), proceedings of the 11th International Workshop on Low Temperature Detectors LTD-11 11th International Workshop on Low Temperature Detectors.

[31] D. J. Goldie, A. V. Velichko, D. M. Glowacka, and S. Withington, Journal of Applied Physics **109**, 084507 (2011).

[32] D. Abrams, D. S. Akerib, M. S. Armel-Funkhouser, L. Baudis, D. A. Bauer, A. Bolozdynya, P. L. Brink, R. Bunker, B. Cabrera, D. O. Caldwell, J. P. Castle, C. L. Chang, R. M. Clarke, M. B. Crisler, R. Dixon, D. Driscoll, S. Eichblatt, R. J. Gaitskell, S. R. Golwala, E. E. Haller, J. Hellmig, D. Holmgren, M. E. Huber, S. Kamat, A. Lu, V. Mandic, J. M. Martinis, P. Meunier, S. W. Nam, H. Nelson, T. A. Perera, M. C. Perillo Isaac, W. Rau, R. R. Ross, T. Saab, B. Sadoulet, J. Sander, R. W. Schnee, T. Shutt, A. Smith, A. H. Sonnenschein, A. L. Spadafora, G. Wang, S. Yellin, and B. A. Young ((CDMS Collaboration)), Phys. Rev. D **66**, 122003 (2002).

[33] N. Anand, A. L. Fitzpatrick, and W. Haxton, (2014), arXiv:1405.6690 [nucl-th].

[34] P. Nadeau, M. Clark, P. Di Stefano, J. C. Lanfranchi, S. Roth, *et al.*, (2014), arXiv:1410.1573 [physics.ins-det].

[35] F. Bellini, M. Biassoni, and et al, arXiv (2010).

[36] R. M. T. Damayanthi, Y. Kunieda, N. Zen, F. Mori, K. Fujita, H. Takahashi, M. Nakazawa, D. Fukuda, and M. Ohkubo, Japanese Journal of Applied Physics **45**, 6259 (2006).

[37] S. J. Smith, J. S. Adams, S. R. Bandler, S. E. Busch, J. A. Chervenak, M. E. Eckart, F. M. Finkbeiner, R. L. Kelley, C. A. Kilbourne, S. J. Lee, J.-P. Porst, F. S. Porter, and J. E. Sadleir, Journal of Low Temperature Physics **176**, 356 (2014).

[38] J. Beeman, F. Bellini, L. Cardani, N. Casali, I. Dafinei, S. D. Domizio, F. Ferroni, F. Orio, G. Pessina, S. Pirro, C. Tomei, and M. Vignati, Astroparticle Physics **35**, 558 (2012).

[39] M. Sisti and et al, in *7th International Workshop on Low-Temperature Detectors LTD7* (2007) pp. 232–236.

[40] S. J. Hart, M. Pyle, and et al, in *THE THIRTEENTH INTERNATIONAL WORKSHOP ON LOW TEMPERATURE DETECTORSLTD13*, Vol. 1185, edited by A. C. Proceedings (2009) pp. 215–218.

[41] Ashcroft and Mermin, “Solid state physics,” (2005).

[42] G. K. White, Proceedings of the Physical Society A **66**, 559 (1953).

[43] Wikipedia,.

[44] R. F. Lang and W. Seidel, arXiv (2009).